Journal of Physics B: Atomic, Molecular and Optical Physics

PAPER

High-order harmonic generation from periodic asymmetric potentials

To cite this article: Tian-Jiao Shao *et al* 2022 *J. Phys. B: At. Mol. Opt. Phys.* **55** 235601

IOP Publishing Journal of Physics B: Atomic, Molecular and Optical Physics
J. Phys. B: At. Mol. Opt. Phys. **55** (2022) 235601 (10pp) https://doi.org/10.1088/1361-6455/ac9e81

High-order harmonic generation from periodic asymmetric potentials

Tian-Jiao Shao[1,2,*], **Huan-Qing Zou**[1,2] **and Qiu-Lan Zhang**[1,2]

[1] School of Information Science and Engineering, NingboTech University, Ningbo 315100, People's Republic of China
[2] Zhejiang University Ningbo Institute of Technology, Ningbo 315100, People's Republic of China

E-mail: shaotj@nit.zju.edu.cn, hqzou@nit.zju.edu.cn and qlzhang@nit.net.cn

Received 21 June 2022, revised 26 September 2022
Accepted for publication 28 October 2022
Published 15 November 2022

Abstract

High-order harmonic generation (HHG) from periodic asymmetric potentials is investigated by solving the real-space time-dependent Schrödinger equations and semi-conductor Bloch equations. Our results show that the periodic asymmetric potential will cause asymmetric excitation and HHG dynamics in the time domain, leading to the signal of even order harmonics. From the *k*-space perspective, a *k*-dependent transition dipole moment phase reflects the real-space asymmetry and causes the symmetry breaking of excitation and HHG dynamics. We also illustrate that the dephasing effect competes with the asymmetry of interband HHG dynamics. Large amplitude of the driving field is beneficial for observing the symmetry breaking of interband HHG. However, it is found symmetry breaking of intraband HHG dynamics is less influenced by dephasing. Moreover, a carrier-envelope phase controlled driving laser field can be utilized as an isolated attosecond pulse gating mechanism for HHG from the periodic asymmetric potentials.

Keywords: periodic asymmetric potentials, high-order harmonic generation, symmetry breaking, time-dependent Schrödinger equations, isolated attosecond pulse gating mechanism

(Some figures may appear in colour only in the online journal)

1. Introduction

With the development of intense mid-infrared (MIR) laser technology [1, 2], solid high-order harmonic generation (HHG) becomes an active topic in recent years. The solid HHG shows different characteristics from its counterpart in gas media: the cut-off energy of crystal HHG has a linear dependence on the amplitude of the laser field, a multi-plateau structure [3, 4], and unique dependence on th ellipticity of the driving field [5–7]. The HHG in different crystals is governed by different mechanisms. One well-known mechanism is the inter- and intraband current model [9]. By using the intense MIR laser as the driving field, the electrons are excited from the valence band to the conduction band, then the electrons/holes are accelerated under the laser field, and finally, the electrons/holes recombine and the interband current is generated. The intraband current is generated by the Bloch oscillations of electrons/holes within the electric band. The inter- and intraband currents contribute together to the crystal HHG and repeat in each half optical cycle of the driving electric field. Recently, HHG in quasicrystals has also been studied [12]. It is found that fractal bands play important roles in these systems. The role of vacancy defect states in solid HHG has also been investigated. It is reported that different vacancies such as boron and nitrogen vacancies cause different defect-induced gap states, which leads to quite different spin-polarized HHG spectra [13].

The application of solid HHG includes the retrieve of the band structure [14], characterizing of the bond information [15], crystal spatial symmetry [16, 17], laser temporal symmetry [18], tomography of the valence potential and electron density in crystals with angstrom spatial resolution and attosecond time resolution [19], and so forth.

* Author to whom any correspondence should be addressed.

In gas HHG, for asymmetric molecules, electrons are preferentially located in deeper wells, and the excitation process is different in the consecutive half cycle [20]. Therefore, due to the broken temporal symmetry, both even and odd harmonics are found in the spectra. This is the result of the interaction between the driving laser and the permanent dipole derived from asymmetric molecules. Similarly, the symmetry breaking phenomenon is possible to be observed when there is a periodic asymmetric structure in crystals. For instance, by tailing the Lissajous figure formed by the two-color circular polarized driving pulse to the symmetry of the graphene lattice, the electronic excitation and higher harmonic generation of valley polarization can be realized, and even order harmonic signals emerged due to the inversion symmetry breaking of adjacent carbon atoms and the asymmetry induced by Valley polarization [21].

HHG in crystals can be well described by numerically solving the time-dependent Schrödinger equation (TDSE) [22, 23] and semi-conductor Bloch equation (SBE) [8–11]. In this work, HHG from the periodic asymmetric potential is investigated. Even order harmonics are observed in both the first and second plateau of HHG spectra. Numerical results show that the excitation and HHG dynamics are asymmetric in time domain from the periodic asymmetric potential. Because a large number of solid targets have non-centrosymmetric structures, the symmetry breaking shown in the HHG from periodic asymmetric potential should be a common phenomenon in strong-field physics in solids.

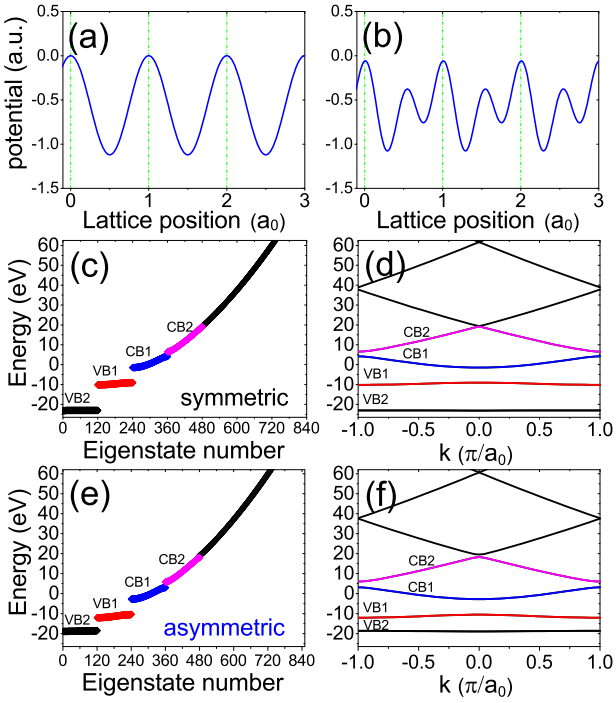

Figure 1. (a) and (b) The blue solid line shows the potential of the one-dimensional periodic symmetric (a) and asymmetric (b) potentials. (c)–(f) The energy band structures of periodic symmetric (c) and (d) and asymmetric (e) and (f) potentials.

2. Theoreitical details

2.1. Time-dependent Schrödinger equations

The eigenvalue and eigenstates of the one-dimensional periodic potential is obtained by solving the eigenvalue equation of $\hat{H}_0$,

$$\hat{H}_0\phi_n(x) = E_n\phi_n(x), \tag{1}$$

where, n is the sequence number of eigenstates and $\Phi_n(x)$ is the corresponding eigen-wavefunction. The above formula is solved numerically by diagonalizing the Hamiltonian $\hat{H}$ in coordinate space. $\hat{H}_0$ is represented by an $N \times N$ matrix and N is the number of spatial grids. The Hamiltonian $\hat{H}_0$ is given by,

$$\hat{H}_0 = \hat{T} + \hat{V}(x) = -\frac{\hbar^2}{2m}\Delta + \hat{V}(x), \tag{2}$$

where $\hat{T}$ is the kinetic energy operator and $\hat{V}(x)$ is the potential energy operator. Atomic units are used in this work. The Mathieu type potentials are used to describe the periodic potential $V(x)$ and the periodic symmetric potential $V_s(x)$ is given by [25],

$$V_s(x) = -V_0\left[1 + \cos\left(2\pi x/a_0\right)\right] \tag{3}$$

where $V_0 = 0.5603$ a.u., and $a_0 = 8$ a.u. is the lattice constant. The periodic asymmetric potential $V_a(x)$ is given by [25],

$$V_a(x) = -V_0[2.5 - \alpha\,\cos(4\pi x/a_0) - \beta\,\cos(2\pi x/a_0 - \phi_r)] \tag{4}$$

where $\alpha = 1.5$ and $\beta = 1.0$ are the parameters controlling the depth of the two wells inside the lattice. $\phi_r = \pi/2$ is the spatial phase term between the two frequency components.

The periodic symmetric potential $V_s(x)$ and asymmetric potential $V_a(x)$ are shown in figures 1(a) and (b), respectively. In figure 1(b), each lattice has a double-well structure. In order to obtain the energy band structure, we solve the equation (1) and the eigenvalue of states is given by,

$$E = \langle\psi|\hat{H}_0|\psi\rangle, \tag{5}$$

where E is the eigenvalue of the states and $\hat{H}_0$ is the field-free Hamiltonian of periodic potentials, respectively. The eigenvalue of both symmetric and asymmetric potential is calculated in coordinate space in the region of 960 a.u. (120 lattices). As shown in figures 1(c) and (e), the states numbered 1–120 and 121–240 represent the valence band 2 (VB2) and valence band 1 (VB1), respectively. While the states numbered 241–360 correspond to the conduction band 1 (CB1).

Figures 1(d) and (f) show the energy band structure in the first Brillouin region ($|k| \leqslant \pi/a_0$) of the symmetric and asymmetric potential solved by the Bloch-state basis expansion method [22, 23]. The energy band structure obtained by two different methods are consistent. The minimum energy band gap between valence band maximum and conduction band minimum is 7.5586 eV and 7.5595 eV for $V_s(x)$ and $V_a(x)$, respectively, to ensure they have close band gap values.

After the eigenstate wavefunction of the valence band and conduction band is obtained by the Bloch-state basis expansion

method, the interband transition dipole moment (TDM) can be determined according to the matrix element of the momentum operator [9],

$$\mathbf{d}(\mathbf{k}) = \langle u_{\mathrm{v}}(\mathbf{k})|\hat{\mathbf{p}}|u_{\mathrm{c}}(\mathbf{k})\rangle \tag{6}$$

According to the above equation, the TDM can be expressed by $\mathbf{d}(\mathbf{k}) = i\int \mathrm{d}^3 u^*_{\mathrm{v},k}(x) \bigtriangledown u^*_{\mathrm{c},k}(x)$ with $u_{m,k}$ being the periodic part of the solution of the Bloch equation. The obtained $\mathbf{d}(\mathbf{k})$ include both the magnitude and phase of TDM, then be used in the semiconductor Bloch equation calculation.

We describe the interaction between a linearly polarized laser and a one-dimensional periodic atomic chain in length gauge, and the time-dependent Hamiltonian is written as,

$$\hat{H} = \hat{H}_0 + xE(t). \tag{7}$$

The time-dependent Schrödinger equation is solved by the split-operator method [26]. All the eigenstates numbered from 121 to 240 filled in valence band 1(VB1) are included as the initial states in the time-dependent calculation. Instead of coupling all states together as a superposition state, each initial state is evolved by TDSE independently. To overcome the nonphysical reflection of the wave function $\psi(t)$ at the edge, an absorption boundary is employed. The solid HHG current is obtained with the time-dependent wave function $\psi(t)$,

$$j(t) = -\langle\psi(t)|\hat{p}|\psi(t)\rangle. \tag{8}$$

The HHG spectra are obtained by calculating the Fourier transform of the laser-induced currents. To analyze the excitation, the time-dependent population (TDP) is obtained as follows [24],

$$|C_n(t)|^2 = \langle\varphi_n|\psi(t)\rangle^2 \tag{9}$$

where φ_n is the field-free state with eigenenergy of E_n. $|C_n(t)|^2$ can be understood as the time-dependent population on the eigenenergy E_n.

2.2. Semiconductor Bloch equations

The electron dynamics within a solid crystal are described by the semiconductor Bloch equations (SBEs) in the reciprocal momentum space, which is written in a two-band model as [9, 10]:

$$\dot{\pi}(K,t) = -\frac{1}{T_2}\pi(K,t) - i\Omega(K,t)N(K,t)\mathrm{e}^{-\mathrm{i}S(K,t)}, \tag{10}$$

$$\dot{n}_{\mathrm{b}}(K,t) = is_{\mathrm{b}}\Omega^*(K,t)\pi(K,t)\mathrm{e}^{-\mathrm{i}S(K,t)} + \mathrm{c.c.}, \tag{11}$$

where $\pi(K,t)$ relates the polarization strength between the CBM and the VBM, later the polarization $p(K,t)$ is determined by $\pi(K,t)$ as,

$$p(K,t) = d(K+A(t))\pi(K,t)\mathrm{e}^{\mathrm{i}S(K)} + \mathrm{c.c.}, \tag{12}$$

where T_2 and $N(K,t)$ are the polarization dephasing time and the population difference between the conduction ($n_{b=c}$) and the valence ($n_{b=v}$) bands, respectively. In our calculations, the dephasing time describing the coherence between these two band states is used as a free parameter and was fixed at $T_2 = 0.5$ o.c. $s_{b=c} = 1$ and $s_{b=v} = -1$ are constants used to describe (from unity) the band populations variation from the initial state of the system where all electrons are in the valence band. $\Omega(K,t) = \mathscr{F}(t)d(K+A(t))$ is the Rabi frequency for a given laser field $E(t)$ (with corresponding vector potential $A(t) = -\int_{-\infty}^{t}\mathscr{F}(t')\mathrm{d}t'$ and transition dipole $d(K)$. Since both the laser field $\mathscr{F}(t)$ and transition dipole $d(K+A(t))$ are vectors, the $\Omega(K,t) = \mathscr{F}_x(t)d_x(K+A(t)) + \mathscr{F}_y(t)d_y(K+A(t)) + \mathscr{F}_z(t)d_z(K+A(t))$. In our case, the laser polarization is along the z-axis, therefore, $\Omega(K,t) = \mathscr{F}_z(t)d_z(K+A(t))$.

$S(K,t) = \int_{t_{\mathrm{b}}}^{t} E_{\mathrm{g}}(K+A(t'))\mathrm{d}t'$ is the classical action for an electron with crystal momenta K transformed into a moving frame $K = K + A(t)$, and E_{g} being the bandgap energy, t_{b} is beginning time of the laser pulse.

2.3. Quasi-classical model

In the quasi-classical model, since the tunneling excitation rate has an exponential dependence on the bandgap, the electrons are supposed to be excited mainly around Γ point which is the eigenstate on top of VB1 in k-space. The motion of electrons in the k-space can be written as follows,

$$k(t) = k_0 + \frac{e}{\hbar}A(t), \tag{13}$$

where k_0 is the initial wave vector at Γ point and $A(t)$ is the vector potential of the driving laser field. When the birth of electrons/holes through tunnel excitation, the electrons/holes does Bloch osillations driven by the laser field. When the electron and holes recounter each other, harmonic photons are emitted with the order given by,

$$\eta(t) = \frac{\varepsilon_{\mathrm{c}}(k(t)) - \varepsilon_{\mathrm{v}}(k(t))}{\hbar\omega_0}, \tag{14}$$

where $\varepsilon_{\mathrm{c}}(k(t))$ and $\varepsilon_{\mathrm{v}}(k(t))$ are the energy of electron and holes, respectively. While ω_0 is the frequency of driving laser field.

3. Results and discussion

3.1. Real space perspective of HHG in periodic asymmetric potential

The shape of the 24-cycle trapezoidal laser pulse is plotted in figure 2(a) which has a total duration of 24 o.c. and a 3 o.c. ramp-up in our calculation. A $E_0 = 0.011$ a.u., 1600 nm driving laser field corresponds to a maximum of vector potential equal to 0.3863 a.u., which is about 98% of the Brillouin zone ($k_{\max} = 0.3927$ a.u.). We can see that in the range from $T = -9T_0$ to $9T_0$ the amplitude of the electric field is identical in each optical cycle. Figure 2(b) shows the solid HHG current driven by the 24-cycle trapezoidal laser pulse.

Figure 2(d) shows the HHG spectra in periodic symmetric (black solid lines) and asymmetric potentials. For periodic asymmetric potentials, the HHG spectra from the driving field with opposite polarization are calculated. Both odd and even order harmonics are observed in the HHG spectra driven by a 24 o.c., trapezoidal, 1600 nm laser field from periodic

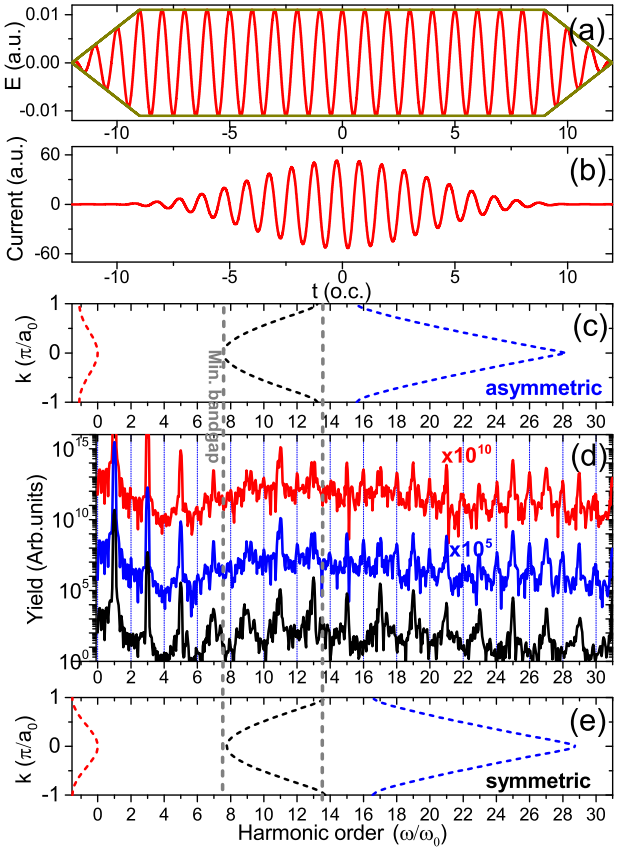

Figure 2. (a) Temporal profile of 24-cycle trapezoidal driving laser pulse. (b) The HHG current obtained by solving the real-space TDSE from the periodic asymmetric potentials. (c) and (f) Band structure of the periodic asymmetric potentials (c) and symmetric potentials (f) guiding the structure of double-plateau characteristics shown in (d). (d) The HHG spectra of the symmetric (black solid line) and periodic asymmetric potentials with parallel (red solid line) and anti-parallel (blue solid line) polarization direction of the driving field. Simulated laser parameters: a field strength $E_0 = 0.011$ a.u., 24-cycle trapezoidal, 1600 nm laser field.

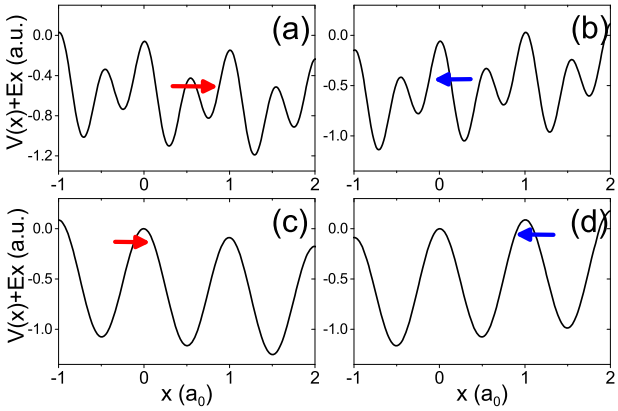

Figure 3. Schematic real-space representation of regimes of HHG in symmetric (a) and (b) and asymmetric (c) and (d) periodic potentials exposed to an oscillating driving electric field. The laser parameters are same as those in figure 2.

asymmetric potential. The HHG spectra show a double-plateau structure, the first plateau starts at $7.8\omega_0$ (minimum bandgap) and ends at $13.5\omega_0$. The second plateau starts at $13.5\omega_0$ and ends at stage around $28.5\omega_0$. For the HHG spectrum in periodic asymmetric potentials, the even-order harmonics are observed from both the first and second plateaus compared with the spectra from the symmetric potential.

An even harmonic at 8th is also observed from HHG spectra in the periodic symmetric potential in figure 2(d). The emergence of even harmonics indicates the dynamic symmetry of the system is broken. This even harmonic signal is considered caused by the indirect transition when the conduction band with higher energy such as CB2 is included in the case of a multi-band system [3, 27].

According to the three-step model of solid HHG [9, 10, 28]: (1) electrons and holes are generated by an intense driving laser field; (2) then electrons/holes oscillate within the energy band driven by the electric field; (3) the electrons and holes recombine with each other and high-order harmonic photons are produced. Thus it is possible to control the HHG dynamics by controlling the excitation step. Similar to the HHG in asymmetric molecules [20], the excitation symmetry will be broken in the periodic asymmetric potential driven by a monochromatic electric field. For the periodic symmetric potential, the polarization direction of the following half cycle of the laser field is opposite, and the laser dressed potential energy thus is inversely symmetric, as shown in figures 3(c) and (d). Therefore, the excitation probability is equal in the adjacent half-optical period. As a result, the HHG processes repeat in each half optical period.

For periodic asymmetric potentials, electrons tend to locate in the deeper potential within the lattice. As shown in figures 3(a) and (b), in the first half optical cycle, the electric field is parallel to the inherent permanent dipole moment of the asymmetric potential, and the energy of the electron is reduced by the downshifting action of the driving laser and the ionization probability of the electron is low [20]. In contrast, in the consecutive half optical period, the laser field is reversed and the excitation rate increases. Therefore, the yield of HHG in the half optical period where the electric field is parallel to the PDM is higher than in the antiparallel case. Therefore, the temporal periodicity of HHG electron dynamics changes from π rad to 2π rad, and even order harmonic signals will be generated.

Figures 4(a) and (b) show the TDP in periodic symmetric potential and asymmetric potential, respectively. The electrons are driven forth and back by the external laser field. In figure 4(a), the period of oscillations of electron population in the energy band corresponds to the half optical cycle of the driving laser. However, in figure 4(b), the time-dependent populations are different between the neighbor half optical cycle in the periodic asymmetric potential showing the asymmetry of the excitation. This agrees with our discussion above.

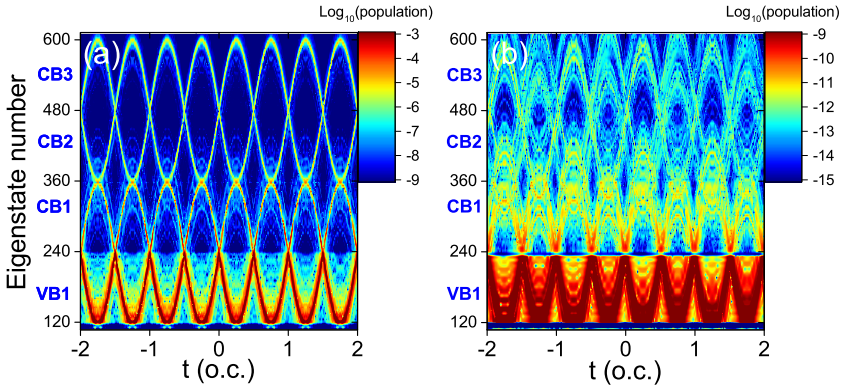

Figure 4. (a) The time-dependent population of the periodic symmetric potential. (b) The time-dependent population of the periodic asymmetric potential.

3.2. Temporal profile of HHG in periodic asymmetric potentials

Figures 5(a)–(d) show the temporal profile of solid HHG from the asymmetric potential and symmetric potential, respectively. The first and second plateaus predicted from the quasi-classical trajectory agree well with the temporal profile of HHG from the TDSE.

One can see the HHG dynamics predicted by the classical model repeat in each half optical period, which is independent of the laser polarization. This is because quasi-classical calculation only requires the band energy while the real space laser-dressed asymmetry of potential or complex transition dipole moment (TDM) phase is ignored.

Figures 5(a) and (b) show the temporal profile of HHG from the periodic asymmetric potentials driven by the laser field with the opposite polarization direction. In figure 5(a), in each optical period, there are one 'strong' ($t = T_0/2 + \mathrm{N}T_0$) and one 'weak' harmonic emission ($t = T_0 + \mathrm{N}T_0$). When the driving laser field changes signs, in figure 5(b), the temporal profile of harmonic emission shifts by half optical cycle, and there is one 'strong' ($t = T_0 + \mathrm{N}T_0$) and one 'weak' harmonic emission ($t = T_0/2 + \mathrm{N}T_0$). This indicates the temporal symmetry breaking of HHG in periodic asymmetric potentials and explains why even order harmonic is observed in figure 2. For comparison, the temporal profile of HHG from the periodic symmetric potentials driven by 24 o.c. trapezoidal laser field with opposite polarization is plotted in figures 5(c) and (d), respectively. One can observe the HHG dynamics have a period of half optical cycle for both the first and second plateaus.

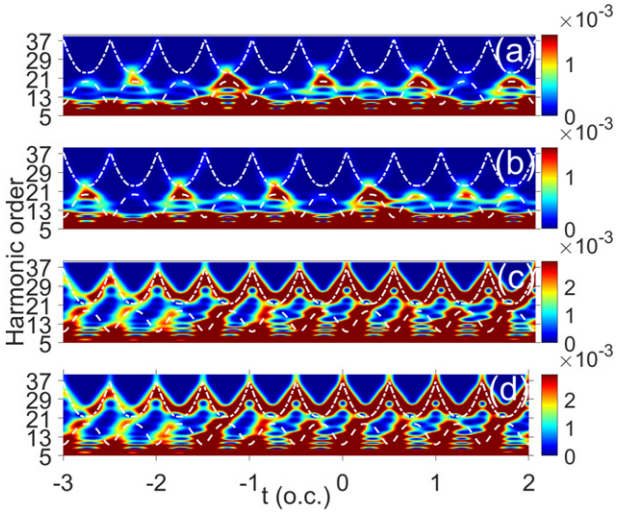

Figure 5. (a) and (b) The temporal HHG profile of eigenstate on top of VB1 in k-space driven by the 24-cycle trapezoidal laser pulse from the periodic asymmetric potentials with parallel (a) and anti-parallel (b) polarization direction of the driving field. (c) and (d) The temporal HHG profile of eigenstate on top of VB1 in k-space driven by the 24-cycle trapezoidal laser pulse from the periodic symmetric potentials with parallel (c) and anti-parallel (d) polarization direction of the driving field.

3.3. k-space perspective

Figure 6(a) shows the amplitude and phase of the TDM from periodic potentials which are solved by the Bloch-state basis expansion method. For both symmetric and asymmetric atomic chains, the corresponding bandgap is the smallest at the Γ point ($k = 0$) which is the eigenstate on top of the valence band. The transition dipole amplitude reaches the peak at the Γ point as shown in figure 6(a). For a one-dimensional periodic symmetric potential with inverse symmetry, the TDM is a real quantity and an even function with respect to k [29, 30]. The TDM phase is a constant with respect to k as shown by the blue solid scatters.

For periodic asymmetric potential, the TDM is a complex quantity. The k-dependent TDM phase plotted by blue-white scatters in figure 6(a) reflects the asymmetry of system in real space and is closely linked to the observed even harmonic signal.

In k-space, the HHG spectra calculated by SBEs [9, 10] are shown in figure 6(b). Here, the Gaussian laser duration is 20 o.c., the wavelength is 3300 nm and the amplitude of field strength E_0 is 0.003 a.u. For the periodic asymmetric potential, clear and sharp even order harmonics can be seen in both HHG contributed by the interband (blue solid line) and intraband (red solid line) transitions. The temporal profile

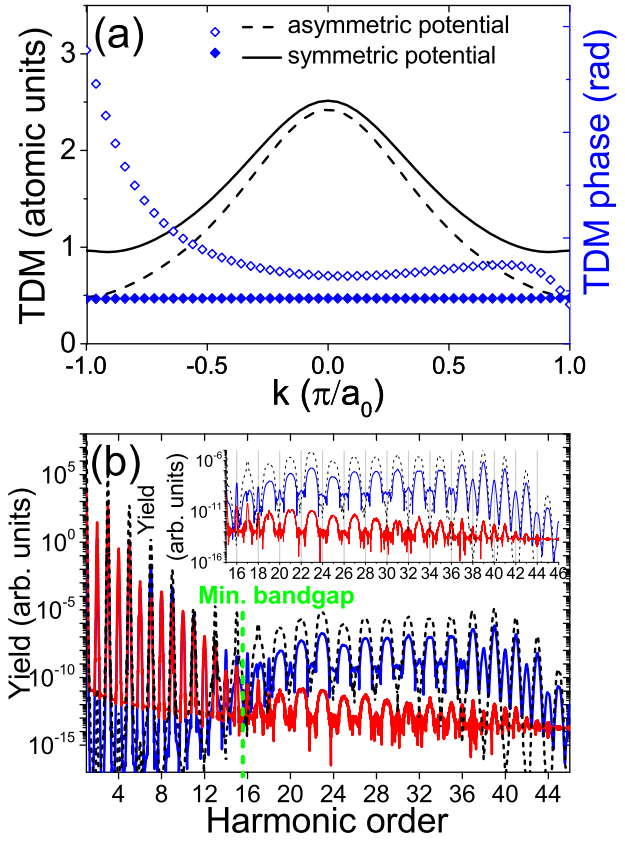

Figure 6. (a) The black solid line and black dashed line show the TDM of the periodic symmetric and asymmetric potentials, respectively. The blue solid scatters and blue-white scatters show the phase of the TDM from the periodic symmetric and asymmetric potentials, respectively. (b) The interband (blue solid line) and intraband contributions (red solid line) of the high-order harmonic generation from the periodic asymmetric potentials solved by SBEs. The black dashed line shows the total HHG spectra with the same simulation parameters except for a constant phase of TDM which is plotted for comparison. A zoom version of the spectra shows the harmonics above the minimum bandgap. Simulated laser parameters: the dephasing time is $T_2 = T_0/4$, full-width-at-half-maximum (FWHM) is 20 o.c., a field strength $E_0 = 0.003$ a.u., the 3300 nm driving laser has a temporal shape of Gaussian function.

of HHG contributed by the interband and intraband transition in figures 7(b) and (c) shows the minimum period of HHG changes to one optical cycle when the TDM phase is a complex quantity. The intrinsic temporal symmetry of the HHG process is broken.

3.4. Dephasing-time effect

In solids, the dephasing time describes the coherence between the electron in the conduction band and the hole in the valence band. A short dephasing time will suppress the high-order recombination trajectories between the electron and hole. As shown in figure 7(a), harmonic emission is mainly contributed by the short trajectory when $T_2 = T_0/4$. Both odd and even order harmonic signal is observed from spectra contributed by interband and intraband transitions. As shown in the temporal profile of interband transition in figure 7(b) due to the asymmetry of excitation, in each optical cycle, there is one 'strong' harmonic emission and one 'weak' harmonic emission in the following consecutive half cycle. Similarly to interband transition, in figure 7(c), the temporal profile of intraband transition also shows only one strong HHG emission in each optical cycle of the driving field.

Figures 7(d), (e) and (f) show harmonic emission by assuming TDM with phase invariable with k, all the other parameters are identical with figures 7(a)–(c). Substantial contrast is observed by assuming a constant TDM phase. One can see from figure 7(a) that only odd harmonics are produced. Both the temporal profile of interband HHG in figure 7(e) and intraband HHG in figure 7(f) are generated twice in each optical cycle of the driving field, therefore the even order harmonics between neighbor consecutive half-cycle cancel each other.

As shown in figures 7(g)–(i), by increasing the dephasing time up to $20T_0$, the intensity of the long trajectory of interband transition becomes stronger and high-order recombination emerges. In figure 7(h), from $t = T_0$ to $2T_0$, the longer dephasing time leads to a harmonic radiation emerge at $t = 1.5T_0$ compared with figure 7(b). The HHG burst is no longer once in each optical cycle. In the corresponding harmonic spectrum, from $16\omega_0$ to $28\omega_0$, the even-order harmonic signal becomes less obvious. The interferences between high-order recombination trajectories in interband transition lead to the suppression of even order signals and are responsible for the loss of clear harmonic structure.

However, in contrast to interband transition, one can find the intraband transition is not very sensitive to the dephasing time. When the dephasing time is increased up to $20T_0$, clear even order harmonics appear in the region in the spectra with energy below the minimum band gap. This might be contributed to the dephasing time describing the coherence between the conduction and valence band, therefore, is directly related to the interband transition. While the intraband transition is mainly related to the excitation process in the three-step model of solid HHG. Thus HHG contributed by the intraband transition is less influenced by the dephasing. The temporal profile of intraband transition in figure 7(i) for $T_2 = 20$ o.c. further confirms this.

As a result, the dephasing time affects the interband and the intraband HHG differently. For interband HHG, dephasing competes with the asymmetry of interband HHG dynamics in solid HHG from periodic asymmetric potentials. When the driving electric field is strong, the dephasing time is short due to the high speed of the electrons. Moreover, a larger electric field will enlarge the asymmetry of excitation in the time domain from periodic asymmetric potentials. It can be expected that the symmetry-breaking effect will become more significant when the amplitude of the driving laser is large. In the second, intraband HHG dynamics are mainly determined by the excitation process and less influenced by the dephasing. Thus even order harmonics below the minimum band gap of periodic asymmetric lattice should be clear and irrelevant to the dephasing.

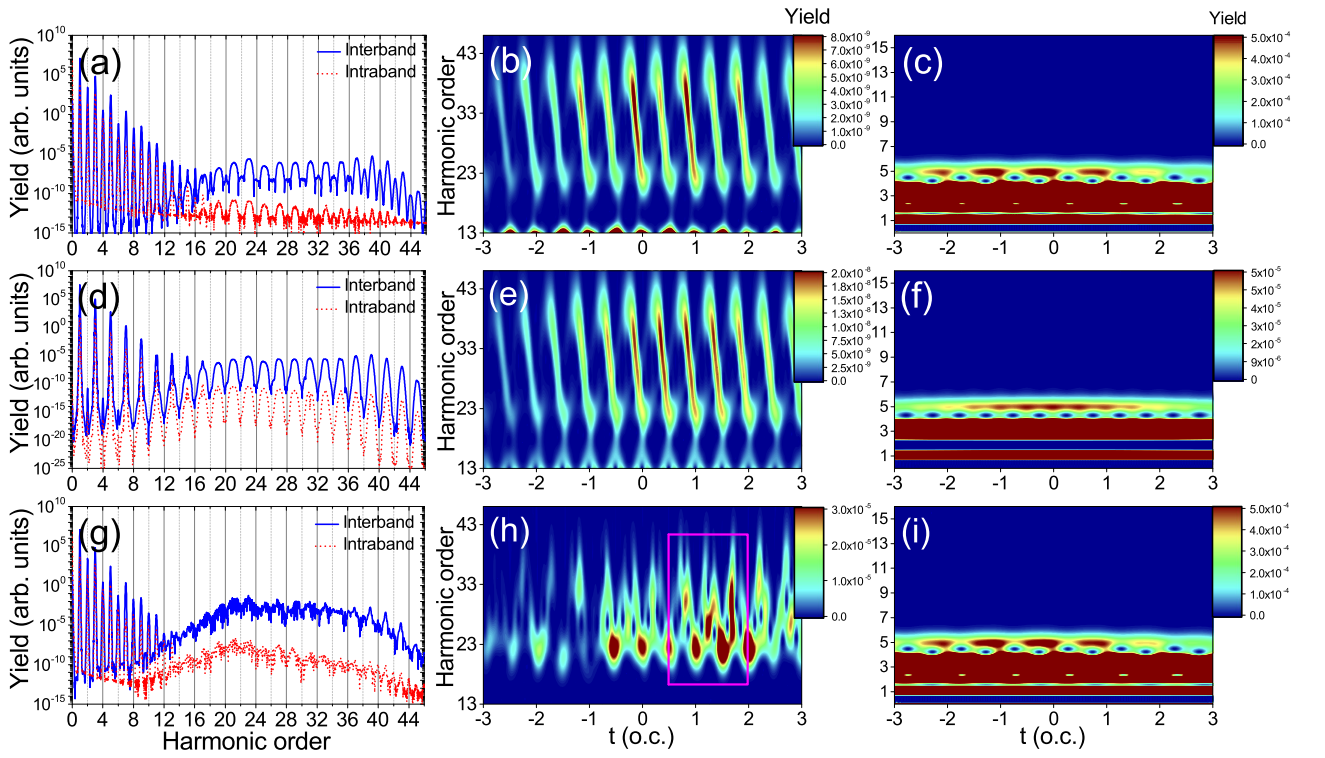

Figure 7. Left column (a), (d) and (g): HHG spectra contributed by interband and intraband transition. Middle column (b), (e) and (h): temporal profile of interband HHG. Right column (b), (d) and (f): temporal profile of intraband HHG. (a)–(c) $T_2 = T_0/4$ with a k-dependent phase of TDM from periodic asymmetric lattice; (d), (e) and (f) same as the upper row by assuming a constant phase of TDM; (g), (h) and (i) $T_2 = 20T_0$ with the k-dependent phase of TDM from the periodic asymmetric lattice. Simulated laser parameters: FWHM is 20 o.c., a field strength $E_0 = 0.003$ a.u., the 3300 nm driving laser has a temporal shape of Gaussian function.

3.5. Carrier-envelope phase dependence

In the following, we study the CE phase dependence of solid HHG in the periodic asymmetric potential by using few-cycle laser pulses. Figure 8(a) shows the temporal waveform of the 3 o.c., 3300 nm, $E_0 = 0.003$ a.u. laser pulses with CE phase $\Phi_{CE} = 0$ and $\Phi_{CE} = \pi$ rad. The two waveforms are identical, except that the polarization direction of the laser is opposite. For inverse symmetric systems, such as inert gas or fused quartz, the driving field with CE phase $\Phi_{CE} = 0$ and $\Phi_{CE} = \pi$ rad will produce the same HHG spectra.

However, in a periodic asymmetric potential, the excitation differs between the consecutive half-optical cycles. For periodic asymmetric potential, the laser-dressed lattice potential is not inverse symmetric. The electron tends to locate in the deeper well of the two-double well structure of the lattice. Therefore, in the former half-cycle, the electric field is parallel to the permanent dipole of the lattice, the electron energy is reduced due to the downshifting action of the driving field. As a result, the excitation probability and harmonic yield are low. In the following consecutive half cycle, the laser field changes sign, the electron energy raises by upshifting action of the laser field, leading to a larger excitation probability and higher harmonic yield.

As shown in figure 8(b), there are obvious differences between the HHG spectra driven by the few-cycle laser field of $\Phi_{CE} = 0$ (red solid line) and $\Phi_{CE} = \pi$ rad (blue dashed-dotted line). In figure 8(c), the harmonic yield is plotted as a function of CE phase from 0 to 3π rad. When the CE phase is varied, the harmonic peaks shift, forming a period in 2π rad of the CE phase rather than a period of π rad for a symmetric system.

Figures 8(d) and (e) show the temporal profile of HHG driven by three-cycle lasers with $\Phi_{CE} = 0$ and $\Phi_{CE} = \pi$ rad, respectively. The half-cycle HHG processes are marked with '1', '2', and '3'. When $\Phi_{CE} = 0$, as shown in figure 8(d), the harmonic bursts '1' and '3' are suppressed, while the harmonic emission burst '2' is enhanced. In contrast, in figure 8(e), for $\Phi_{CE} = \pi$ rad, harmonic pulse '2' is suppressed, while harmonic pulses '1' and '3' are enhanced. This explains the difference between HHG spectra driven by a few-cycle laser pulse with a π phase shift of CE phase in figure 8(b).

In figure 8(d), the enhanced harmonic burst '2' indicates an isolated attosecond emission can be selected. In figure 8(f), a synthesized 977-as isolated attosecond pulse (IAP) is shown by superposing harmonics from 27th to 37th from HHG emission driven by few-cycle pulse with CE phase $\Phi_{CE} = 0$ without any phase compensation (red solid line). However, when CE phase $\Phi_{CE} = \pi$ rad, 2 as bursts are synthesized rather than the IAP (blue dashed-dotted line). This indicates excitation and HHG dynamics in asymmetric lattice potential can be exploited as a gating mechanism for the generation of IAP by choosing a proper polarization direction of the driving laser field.

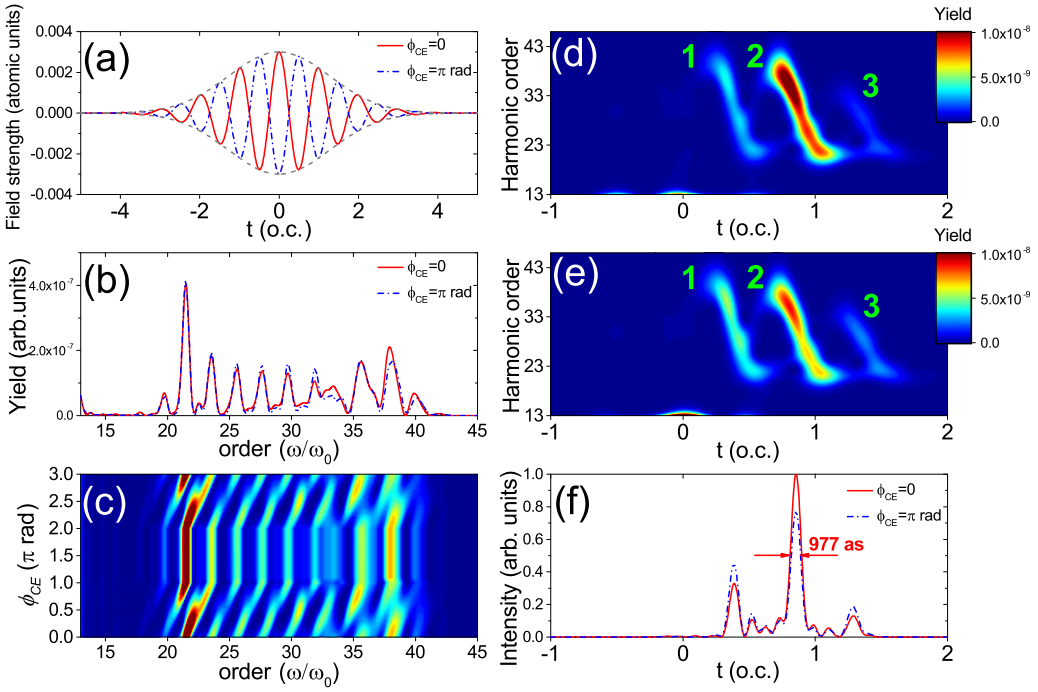

Figure 8. (a) Temporal profile of 3 o.c. gaussian driving laser pulse with CE phase $\Phi_{\rm CE} = 0$ (red solid line) and $\Phi_{\rm CE} = \pi$ rad (blue dashed-dotted line). (b) The HHG spectra for two different CEP values of $\Phi_{\rm CE} = 0$ and $\Phi_{\rm CE} = \pi$ rad. (c) Calculated CEP dependence of HHG from periodic asymmetric potential. (d) and (e) The temporal HHG profile for $\Phi_{\rm CE} = 0$ (d) and $\Phi_{\rm CE} = \pi$ rad (e). (f) The temporal profile of the synthesized IAP. The IAP is synthesized by inverse Fourier transforming the harmonics from the 27th to 37th order. Simulated laser parameters: the dephasing time is given as $T_2 = T_0/4$, FWHM is 3 o.c., a field strength $E_0 = 0.003$ a.u., the 3300 nm driving laser has a temporal shape of Gaussian function.

4. Conclusion

The purpose of this paper is to study the solid HHG process in periodic asymmetric potentials. Firstly, driven by a monochromatic multi-cycle 1600 nm laser pulse, even harmonics are observed from the solid HHG spectra. Our real-space TDSE simulation confirms the temporal symmetry breaking of the excitation and HHG dynamics leading to the even order signal observed from the HHG spectra.

In addition, by using the Bloch state expansion method, the TDM of the periodic asymmetric potential is obtained. The TDM in the asymmetric system is a complex quantity and the k-dependent phase reflects the asymmetry of real space structure. We also find that the dephasing effect competes with the temporal symmetry breaking of interband contributed HHG. By increasing the amplitude of the driving field, the even-order harmonic signal is expected to be more obvious. This is because the asymmetry of excitation will increase and the high-order recombination trajectory will be suppressed by a short dephasing time when the driving electric field is strong. While the intraband HHG is less influenced by dephasing time.

Finally, we further extend the analysis to the CE phase controlled HHG dynamics in periodic asymmetric potentials. The minimum periodicity of HHG dependence on CE phase is 2π rad in periodic asymmetric potentials rather than the π rad for HHG in the symmetric system. By employing a CE phase-modulated driving field, the quantum path of the HHG process from periodic asymmetric potentials can be effectively selected and is promising to be utilized as an isolated attosecond pulse gating mechanism.

Acknowledgments

We thank Professor Xue-Bin Bian for the discussions. This work was supported by the Zhejiang Provincial Natural Science Foundation of China (No. LQ22A040004), Ningbo Natural Science Foundation (No. 2021J153), and the National Natural Science Foundation of China (No. 12104395).

Data availability statement

The data that support the findings of this study are available upon reasonable request from the authors.

Appendix

The band dispersion curves in the reciprocal space are originally computed from Bloch-state basis expansion method and fitted by the Fourier series,

$$E_{\rm CB}(k_x) = \sum_{j=0}^{\infty} \alpha_{\rm CB}^{j} \cos(jk_x a_x) \tag{15}$$

Table 1. Bands expansion coefficients of the periodic asymmetric potential.

j	$\alpha_{\rm VB}$	$\alpha_{\rm CB}$
α_0	−11.33	−0.3018
α_1	0.7597	−2.749
α_2	0.03791	0.3903
α_3	0.004122	−0.1572
α_4	0.0007473	0.06797
α_5	-5.104×10^{-5}	−0.03535
α_6	1.081×10^{-4}	0.02003
α_7	-7.202×10^{-5}	−0.01234
α_8	5.995×10^{-5}	0.008159
α_9	-4.966×10^{-5}	−0.005751
α_{10}	4.261×10^{-5}	0.004295

Table 2. The expansion coefficients of the TDM of the periodic asymmetric potential.

j	$\alpha_{\rm dreal}$	$\beta_{\rm dreal}$	$\alpha_{\rm dimag}$	$\beta_{\rm dimag}$
$j=0$	0.414	0.0	−1.178	0.0
$j=1$	0.101	−0.1259	−1.062	−0.07458
$j=2$	−0.01557	0.07514	−0.03992	0.07865
$j=3$	0.02843	−0.05316	−0.1172	−0.06973

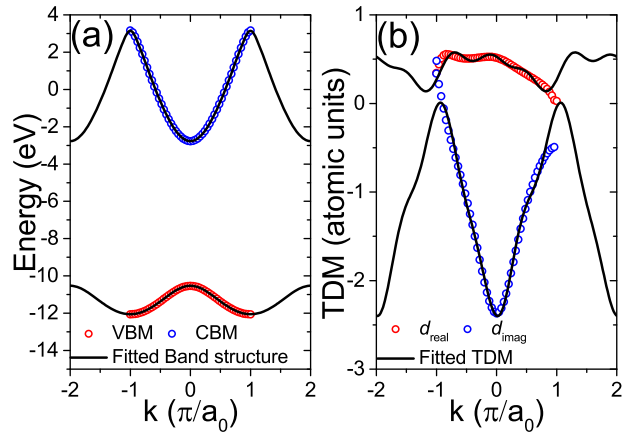

Figure 9. (a) Energy bands of the periodic asymmetric potential. (b) The magnitude of real part $d_{\rm real}$ and imaginary part $d_{\rm imag}$ of the TDM between valence and conduction band considered in the SBE. The black solid line shows the energy bands and TDM fitted by the Fourier series.

$$E_{\rm VB}(k_x)=\sum_{j=0}^{\infty}\alpha_{\rm VB}^{j}\cos(jk_xa_x) \tag{16}$$

where $a_x=8.0$ Bohr is the length of the lattice and k_x is the Bloch vector. We use j up to $n=10$ to expand the energy band dispersion curves. The coefficients can be found in table 1.

The TDM for the periodic asymmetric potential is,

$$d(k_x)=d_{\rm real}(k_x)+id_{\rm imag}(k_x) \tag{17}$$

The real part and imaginary part of TDM are fitted by the Fourier series, respectively,

$$d_{\rm real}(k_x)=\sum_{j=0}^{\infty}\alpha_{\rm real}^{j}\cos(jk_xa_x)+\sum_{j=0}^{\infty}\beta_{\rm real}^{j}\sin(jk_xa_x) \tag{18}$$

$$d_{\rm imag}(k_x)=\sum_{j=0}^{\infty}\alpha_{\rm real}^{j}\cos(jk_xa_x)+\sum_{j=0}^{\infty}\beta_{\rm real}^{j}\sin(jk_xa_x) \tag{19}$$

The coefficients can be found in table 2. The laser polarization is chosen to be along the direction of periodic asymmetric potentials. The SBEs are solved by the finite difference method with 300 k-space points (full Brillouin zone). The energy bands and TDM are displayed in figures 9(a) and (b), respectively.

ORCID iDs

Tian-Jiao Shao https://orcid.org/0000-0001-5178-4544
Qiu-Lan Zhang https://orcid.org/0000-0002-3153-3577

References

[1] Dubietis A, Jonušauskas G and Piskarskas A 1992 *Opt. Commun.* **88** 437–40
[2] Ishii N, Kaneshima K, Kitano K, Kanai T, Watanabe S and Itatani J 2014 *Nat. Commun.* **5** 3331
[3] Ndabashimiye G, Ghimire S, Wu M, Browne D A, Schafer K J, Gaarde M B and Reis D A 2016 *Nature* **534** 520–3
[4] You Y S *et al* 2017 *Opt. Lett.* **42** 1816–9
[5] Yoshikawa N, Tamaya T and Tanaka K 2017 *Science* **356** 736–8
[6] Tancogne-Dejean N, Mücke O D, Kärtner F X and Rubio A 2017 *Nat. Commun.* **8** 745
[7] Wang X Q and Bian X B 2021 *Phys. Rev.* A **103** 053106
[8] Meier T, vol Plessen G, Thomas P and Koch S W 1994 *Phys. Rev. Lett.* **73** 2638
[9] Vampa G, McDonald C R, Orlando G, Klug D D, Corkum P B and Brabec T 2014 *Phys. Rev. Lett.* **113** 073901
[10] Vampa G, McDonald C R, Orlando G, Corkum P B and Brabec T 2015 *Phys. Rev.* B **91** 064302
[11] Li J, Zhang X, Fu S, Feng Y, Hu B and Du H 2019 *Phys. Rev.* A **100** 043404
[12] Liu J Q and Bian X B 2021 *Phys. Rev. Lett.* **127** 213901
[13] Mrudul M, Tancogne-Dejean N, Rubio A and Dixit G 2020 *npj Comput. Mater.* **6** 1–9
[14] Vampa G, Hammond T J, Thiré N, Schmidt B E, Légaré F, McDonald C R, Brabec T, Klug D D and Corkum P B 2015 *Phys. Rev. Lett.* **115** 193603
[15] You Y S, Reis D A and Ghimire S 2017 *Nat. Phys.* **13** 345–9
[16] Saito N, Xia P, Lu F, Kanai T, Itatani J and Ishii N 2017 *Optica* **4** 1333–6
[17] Chen Z Y and Qin R 2019 *Opt. Express* **27** 3761–70
[18] Neufeld O, Podolsky D and Cohen O 2019 *Nat. Commun.* **10** 405
[19] Lakhotia H, Kim H, Zhan M, Hu S, Meng S and Goulielmakis E 2020 *Nature* **583** 55–9
[20] Lan P, Lu P, Cao W, Li Y and Wang X 2007 *Phys. Rev.* A **76** 021801
[21] Mrudul M S, Jiménez-Galán Á, Ivanov M and Dixit G 2021 *Optica* **8** 422–7
[22] Wu M, Ghimire S, Reis D A, Schafer K J and Gaarde M B 2015 *Phys. Rev.* A **91** 043839

[23] Guan Z, Zhou X X and Bian X B 2016 *Phys. Rev.* A **93** 033852
[24] Huang T, Zhu X, Li L, Liu X, Lan P and Lu P 2017 *Phys. Rev.* A **96** 043425
[25] Mrudul M S, Pattanayak A, Ivanov M and Dixit G 2019 *Phys. Rev.* A **100** 043420
[26] Feit M D, Fleck J A and Steiger A 1982 *J. Comput. Phys.* **47** 412–33
[27] Jia G R, Huang X H and Bian X B 2017 *Opt. Express* **25** 23654–62
[28] Du T Y and Bian X B 2017 *Opt. Express* **25** 151–8
[29] Jiang S, Chen J, Wei H, Yu C, Lu R and Lin C D 2018 *Phys. Rev. Lett.* **120** 253201
[30] Jiang S, Wei H, Chen J, Yu C, Lu R and Lin C D 2017 *Phys. Rev.* A **96** 053850

Web of Science™ Core Collection

经检索《Web of Science™ Core Collection》，下述论文被《SCI - Expanded》收录。（数据获取：2022年11月28日）

标题:High-order harmonic generation from periodic asymmetric potentials

作者:Shao, TJ(Shao, Tianjiao) Zou, HQ(Zou, Huanqing) Zhang, QL(Zhang, Qiulan)

来源出版物:JOURNAL OF PHYSICS B-ATOMIC MOLECULAR AND OPTICAL PHYSICS **卷**:55 **期**:23 **文献号**:235601

出版时间:2022,DEC 7 **DOI**:10.1088/1361-6455/ac9e81

出版商:IOP Publishing Ltd **出版商地址**:TEMPLE CIRCUS, TEMPLE WAY, BRISTOL BS1 6BE, ENGLAND

文献类型:Article **语种**:English

入藏号:WOS:000885139800001 **IDS号**:6H0KJ

地址:[Shao, Tian-Jiao; Zou, Huan-Qing; Zhang, Qiu-Lan] Ningbo Tech Univ, Sch Informat Sci & Engn, Ningbo 315100, Peoples R China; [Shao, Tian-Jiao; Zou, Huan-Qing; Zhang, Qiu-Lan] Zhejiang Univ, Ningbo Inst Technol, Ningbo 315100, Peoples R China

通讯作者:Shao, TJ (通讯作者)，Ningbo Tech Univ, Sch Informat Sci & Engn, Ningbo 315100, Peoples R China.; Shao, TJ (通讯作者)，Zhejiang Univ, Ningbo Inst Technol, Ningbo 315100, Peoples R China.

电子邮件:shaotj@nit.zju.edu.cn; hqzou@nit.zju.edu.cn; qlzhang@nit.net.cn

ISSN:0953-4075 **电子ISSN**:1361-6455

ISO 来源文献缩写:J. Phys. B-At. Mol. Opt. Phys. **来源出版物页码计数**:10

注：

以上检索结果均得到被检索人的确认。本证明编号：NBT-SCIE-2022-4521

《SCI - Expanded》检索结果（收录情况）

浙大宁波理工学院图书馆

检索人(签名):

审核人(签章):

2022年12月09日

InCites™ Journal Citation Reports®

经检索《Web of Science™》的JCR数据库，期刊《JOURNAL OF PHYSICS B-ATOMIC MOLECULAR AND OPTICAL PHYSICS》2021年JCR的影响因子情况：

ISSN：0953-4075

eISSN：1361-6455

2021年影响因子：1.655

PHYSICS, ATOMIC, MOLECULAR & CHEMICAL：Q3

OPTICS：Q4

注：

1.以上检索结果均得到被检索人的确认。证明编号：NBT-SCIE-2022-4521-IF2021

2.论文的期刊影响因子应与该论文所发表期刊的年份相对应。

3.因JCR的最新数据截至到2021年，2022年出版论文的期刊影响因子以2021年的期刊影响因子为参考。

《JOURNAL CITATION REPORTS（JCR）》检索结果

浙大宁波理工学院图书馆

检索人(签名)：

审核人(签章)：

2022年12月09日